nature physics

Article

https://doi.org/10.1038/s41567-024-02751-2

Observation of a finite-energy phase transition in a one-dimensional quantum simulator

Received: 2 February 2024

Accepted: 3 December 2024

Published online: 17 January 2025

Check for updates

Alexander Schuckert[1,3] ✉, Or Katz[2,3] ✉, Lei Feng[2], Eleanor Crane[1], Arinjoy De[1], Mohammad Hafezi[1], Alexey V. Gorshkov[1] & Christopher Monroe[2]

Equilibrium phase transitions in many-body systems have been predicted and observed in two and three spatial dimensions but have long been thought not to exist in one-dimensional systems. It was suggested that a phase transition in one dimension can occur in the presence of long-range interactions. However, an experimental realization has so far not been achieved due to the requirement to both realize interactions over sufficiently long distances and to prepare equilibrium states. Here we demonstrate a finite-energy phase transition in one dimension by implementing a long-range interacting model in a trapped-ion quantum simulator. We show that finite-energy states can be generated by time-evolving initial product states and letting them thermalize under the dynamics of a many-body Hamiltonian. By preparing initial states with different energies, we study the finite-energy phase diagram of a long-range interacting quantum system. We observe a ferromagnetic equilibrium phase transition as well as a crossover from a low-energy polarized paramagnet to a high-energy unpolarized paramagnet, in agreement with numerical simulations. Our work presents a scheme for preparing finite-energy states in quantum simulation platforms, enabling access to phases at finite energy density.

Equilibrium phase transitions underlie many quantum phenomena in nature, from the creation of primordial fluctuations in the early universe[1,2] to the melting of confined hadrons into the quark–gluon plasma[3] and the emergence of a superconducting state at high temperatures in the cuprates[4]. Equilibrium phase transitions require the presence of both ordered and disordered phases[5], which have been observed in two and three spatial dimensions. In one-dimensional (1D) systems, disordered phases often have a lower free energy than ordered ones, leading to the absence of phase transitions. This is because the entropy gained by destroying the order is larger than the energy cost[6,7]. More than half a century ago, Dyson and Thouless argued that this energy cost can outweigh the entropy gain if the interactions are sufficiently long-ranged[8,9]. However, despite the extensive theoretical work on phase transitions in 1D long-range systems since these seminal works[10], an experimental realization of this prediction has so far not been achieved. Recently, the advent of quantum simulators has enabled the study of highly controlled long-range interacting systems. This has led to the discovery of many exotic quantum phenomena, including non-local spreading of quasiparticles[11], dynamical quantum phase transitions[12,13], time

[1]Joint Quantum Institute and Joint Center for Quantum Information and Computer Science, University of Maryland and NIST, College Park, MD, USA. [2]Duke Quantum Center, Department of Physics and Electrical and Computer Engineering, Duke University, Durham, NC, USA. [3]These authors contributed equally: Alexander Schuckert, Or Katz. ✉e-mail: schuckertalexander@gmail.com; or.katz@duke.edu

https://doi.org/10.1038/s41567-024-02751-2

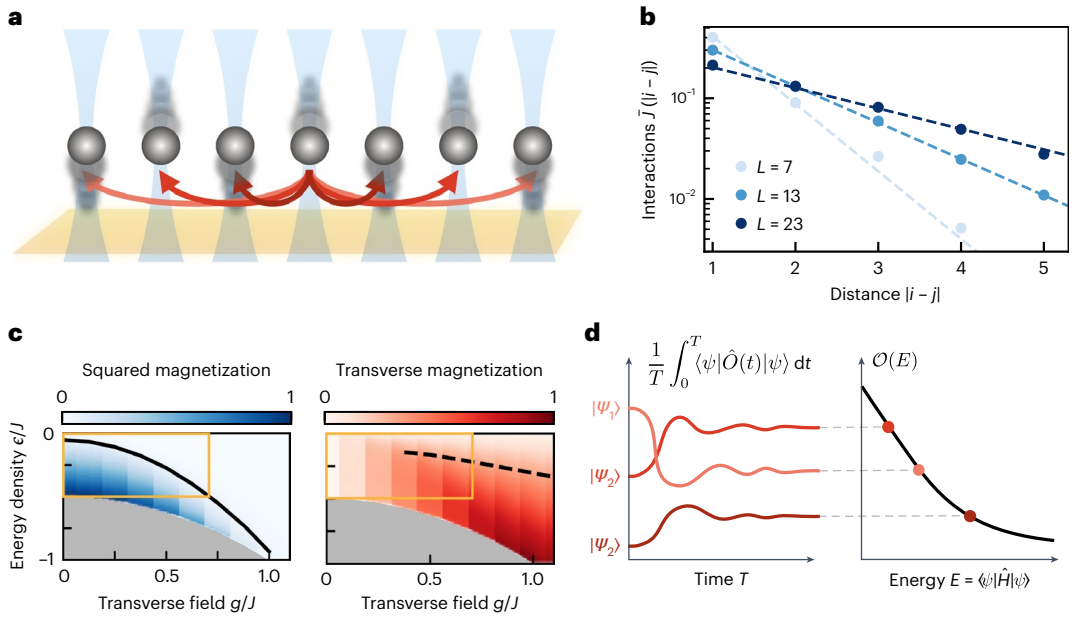

Fig. 1 | Observing an equilibrium phase transition in a 1D chain of ions. a, Ions are confined in a chain using a chip trap (yellow). Individual Raman laser beams (blue) couple an internal spin-1/2 degree of freedom of the ions to the lowest-energy motional mode of the ion crystal (grey), mediating exponentially decaying interactions between the spins (red). **b**, The averaged interactions $\bar{J}(\bar{l}) = \frac{1}{L-\bar{l}}\sum_i J_{i,i+\bar{l}}/(2J\mathcal{N})$ evaluated with the experimental J_{ij} (dots), compared with the target $J_{ij} = J\exp(-\frac{10.8}{L}|i-j|)$ (dashed lines). The experimental J_{ij} are slightly inhomogeneous (Methods and Extended Data Fig. 1). **c**, Equilibrium phase boundary of the model in equation (1) (solid line), as well as the squared magnetization (blue shading) and transverse magnetization (red shading; dashed line indicates where transverse magnetization is equal to 0.75). We extrapolated to the infinite-system-size limit from finite-size MPS simulations. The grey area indicates energies with no states. The gold frame is the regime experimentally probed in this work. **d**, The time-averaged expectation value of a time-evolved local observable at late times gives an estimate for the equilibrium expectation value at the energy of the initial state. Repeating this experiment for initial states with different energy results in an estimate for the value of the observable in equilibrium as a function of energy.

crystals[14,15], continuous symmetry breaking[16,17], supersolidity[18,19] and superdiffusive spin transport[20]. Among the experimental platforms used in those studies, only trapped ions have interactions that are in principle long-range enough to observe an equilibrium phase transition in one dimension. However, preparing equilibrium states in spin-system quantum simulators such as trapped ions and even digital quantum computers has been challenging[21–30]. This is because it is extremely challenging to bring these systems in contact with an external bath with a well-defined finite temperature; instead, the coupling with baths naturally present in the experimental environment either projects the system into an infinite temperature state or onto a trivial product state.

Here, we overcome this challenge by using the intrinsic many-body equilibration within subsystems of isolated quantum systems to prepare equilibrium states in a long-range interacting quantum system realized by trapped ions. Our method relies on the foundational understanding of quantum thermalization offered by the eigenstate thermalization hypothesis (ETH)[31,32], whose validity and limitations have been studied both numerically[32] and experimentally[33,34]. We first prepare non-equilibrium states at a range of different energies and let these states thermalize under the dynamics of a 1D many-body Hamiltonian with programmable long-range interactions. We then use these thermalized states to measure the order parameters of ferromagnetic and paramagnetic phases as a function of energy density. Compared with other schemes[21–30,35,36], this method is relatively simple and does not require two-qubit gates. Thus, it can be implemented in an entirely analogue setting. Moreover, it is widely believed that thermalization times are independent of system size for most observables[37], rendering this method scalable. This enables us to study the existence of a possible equilibrium phase transition in a 1D spin system realized by a trapped-ion analogue quantum simulator.

Realizing a long-range interacting many-body system

In our experiment, we encode a pseudo-spin 1/2 in the electronic ground-state levels $|\uparrow\rangle = |F=1, M=0\rangle$ and $|\downarrow\rangle = |F=0, M=0\rangle$ of $^{171}Yb^+$ ions confined in a linear Paul trap on a chip[38], as illustrated in Fig. 1a. We apply a tightly focused individual addressing beam on each ion and a globally addressing wide beam on all ions to drive the transition between the spin levels via a stimulated Raman process. These transitions couple off-resonantly to the phonon modes of the ion chain, driving simultaneously and nearly symmetrically the red and blue sideband transitions, resulting in effective Ising interactions between the spins. We realize interactions that decay exponentially with ion separation distance by choosing a Raman beat-note frequency that has a detuning from the carrier frequency that is close to the lowest radial phonon-mode frequency. In our experiment, this leads to a longer coherence time than the one obtained by choosing a detuning close to the highest radial mode frequency. We then remove the alternating sign of the interactions by spatially staggering the phases of the Raman beams (Methods). Control over the optical frequencies of the individual beams sets an effective magnetic field in the transverse direction[39,40]. In total, this approximately realizes the many-body spin Hamiltonian

$$\hat{H} = -\frac{1}{2\mathcal{N}}\sum_{i<j} J_{ij}\hat{\sigma}_i^x\hat{\sigma}_j^x - g\sum_i \hat{\sigma}_i^z, \qquad (1)$$

where $\hat{\sigma}_i^\alpha$ are the Pauli matrices, g is the transverse-field strength and i and j run over integers from 1 to L for an ion chain of length L. Due to the Raman beat-note frequency being tuned close to the lowest frequency mode, the interactions decay exponentially with the distance between ions. Although finite-temperature phase transitions are possible in fully connected systems and in systems with interactions that decay as a power law, such transitions do not occur in systems with

https://doi.org/10.1038/s41567-024-02751-2

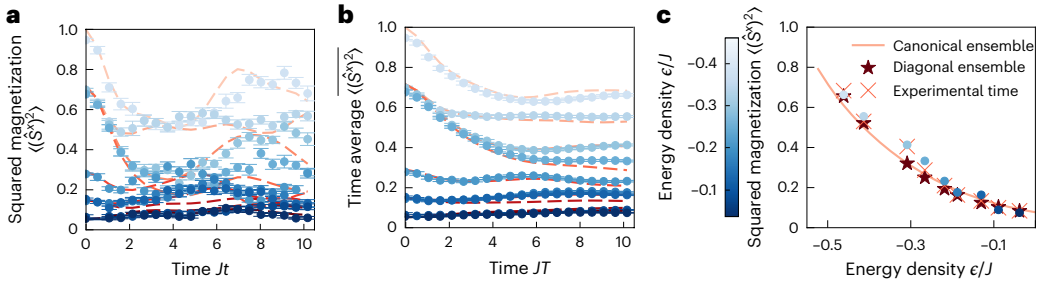

Fig. 2 | Verification of equilibration. a, Time-evolved squared magnetization in the experiment (dots) and numerical simulations (dashed lines). A total of 250 repetitions were taken per data point. The initial states are listed in Extended Data Table 1. **b**, The time average (up to time T) of the time-evolved squared magnetization using the data from **a** (dots) and the corresponding numerical data (dashed lines), evaluated according to equation (2). The colour bar indicates the energy density of the initial states. **c**, A comparison of the latest-time experimental data points from **b** (dots) and the numerical data evolved until the experimental time (crosses) and to infinite time, that is, the diagonal ensemble (stars, evaluated according to the right-hand side in equation (2)). The expectation from the canonical ensemble is shown as a solid line. The numerics use the experimentally realized interactions (Methods). $L = 13, g = 0.3J$. The error bars for the experimental data in **a** and **b** are from a jackknife binning analysis (see, for example, ref. 50). We do not show error bars in **c** as systematic errors due to finite evolution time dominate.

exponential interaction decay[8,9]. To engineer a phase transition in our system, we decrease the decay rate of the interactions with increasing system size by choosing $J_{ij} \approx J \exp(-\frac{\gamma}{L}|i-j|)$ (Fig. 1b). This effectively gives our system the characteristics of a long-range interacting model. To render the energy extensive, we use the Kac normalization procedure[41] by rescaling the overall prefactor of the Hamiltonian by $\mathcal{N} = \frac{1}{L-1}\sum_{i<j}(J_{ij}/J)$. Our choice of $\gamma = 10.8$ results from the need to be sufficiently detuned from the lowest energy mode for the largest system size (giving a lower limit on γ) while still having a strong enough coupling to the modes for the smallest system size so that the dynamics are faster than decoherence (resulting in an upper limit on γ).

To confirm that the Hamiltonian in equation (1) exhibits an equilibrium phase transition, we use matrix product state simulations (Methods). Indeed, for $g \leq J$, we find a low-energy ferromagnetic phase, characterized by a non-zero squared magnetization $\langle \hat{S}_x^2 \rangle \equiv \sum_{ij}\langle \hat{\sigma}_i^x \hat{\sigma}_j^x \rangle / L^2$ (Fig. 1c). The paramagnet outside this ordered phase consists of two regions that are connected by a crossover: at low energies, the system is polarized along the transverse field, while at high energies both the transverse magnetization $\langle \hat{S}_z \rangle \equiv \sum_i \langle \hat{\sigma}_i^z \rangle / L$ and the squared magnetization vanish, and the system is effectively in an unpolarized mixed state. While we expect the universality class to be given by the all-to-all connected model $\gamma = 0$, we numerically found that the critical temperature depends on γ (Extended Data Fig. 4).

Probing finite-energy states in a quantum simulator of spins

Our goal is to study the equilibrium phase diagram in Fig. 1c in a trapped-ion simulator. However, the preparation of equilibrium states by thermalization with an external bath is challenging in spin-system simulators such as trapped ions. This is due to the existence of noise sources whose effect can be modelled as a coupling to an infinite temperature bath, which leads to a trivial non-equilibrium steady state. Instead, we use the fact that subsystems of a many-body quantum system thermalize under the system's own dynamics due to the ETH[31]: the expectation values of local observables $\langle n|\hat{O}|n\rangle$ with respect to eigenstates $|n\rangle$ of chaotic many-body Hamiltonians coincide with their value in the microcanonical ensemble $\mathcal{O}(E_n)$, evaluated at the corresponding eigenenergy E_n. When starting from an initial state $|\psi\rangle$ with an average energy $E = \langle\psi|\hat{H}|\psi\rangle$, the time-averaged observable until time T

$$\overline{\langle\psi|O(\hat{t})|\psi\rangle} \equiv \frac{1}{T}\int_0^T \mathrm{d}t \langle\psi|O(\hat{t})|\psi\rangle \overset{T\to\infty}{\to} \sum_n |\langle n|\psi\rangle|^2 \langle n|\hat{O}|n\rangle \qquad (2)$$

therefore coincides with the microcanonical ensemble $\mathcal{O}(E)$ if the energy-density variance of the initial state $(\langle\psi|\hat{H}^2|\psi\rangle - \langle\psi|\hat{H}|\psi\rangle^2)/L^2$ vanishes as $L \to \infty$, that is if it fulfils the condition for a proper thermodynamic ensemble. This condition is fulfilled for most physical initial states[32] and, in these cases, $|\langle n|\psi\rangle|^2$ is called the diagonal ensemble. The ETH therefore motivates the following simple prescription to evaluating equilibrium observables (Fig. 1d): we prepare initial states with different energies E and evolve them to sufficiently late times while measuring the observable $\hat{O}$. Finally, we record the time-averaged late-time observables on the left-hand side of equation (2) as a function of E as the resulting estimate for $\mathcal{O}(E)$.

The energy range that can be probed in this scheme depends on the initial states $|\psi\rangle$. We use product states in the $\hat{\sigma}^x$ basis. They are the eigenstates of the Hamiltonian for vanishing transverse field $g = 0$. The lowest-energy state is the maximally polarized state, and the energy density is mainly controlled by the number of spin flips. These product states cover a large range of energies even for non-vanishing g/J, indicated by the horizontal edges of the gold frame in Fig. 1c. The energy-density variance of these product states is given by g^2/L, therefore also fulfilling the requirement on $|\langle n|\psi\rangle|^2$ imposed by the ETH.

To test the practical operation of our scheme, we measure the squared magnetization as a function of time for several product initial states for a chain of $L = 13$ spins (Fig. 2a, dots). We find excellent agreement with the numerical solution (dashed lines), which does not include experimental imperfections except the inhomogeneity of the interactions. In Extended Data Fig. 2, we also measure the time evolution of the energy, showing that it is approximately constant as expected in a closed system. Evaluating the time average in equation (2), we find an approximate convergence with the averaging time T for $JT \gtrsim 8$. Finally, we show the latest-time values of the time-averaged squared magnetization in Fig. 2c, along with the numerical results from time evolving to the same time as the experiment (crosses) and to infinite time (diagonal ensemble, stars). The canonical ensemble is shown as a solid line. We find good agreement between the equilibrium diagonal ensemble (which itself is in good agreement with the canonical ensemble) and the experimental data with at most 0.04 absolute error between the experiment and the diagonal ensemble. We attribute the deviations mainly to the finite experimental evolution time (Extended Data Figs. 7–9), with further imperfections studied in Extended Data Fig. 3. We note that, for large g/J, the thermalization time increases radically due to the presence of a dynamical quantum phase transition[13] (Methods). In our studied range of small-to-moderate g/J, the good agreement of time-evolved observables with equilibrium ensembles confirms that our scheme enables the evaluation of equilibrium observables on timescales accessible to the experiment.

https://doi.org/10.1038/s41567-024-02751-2

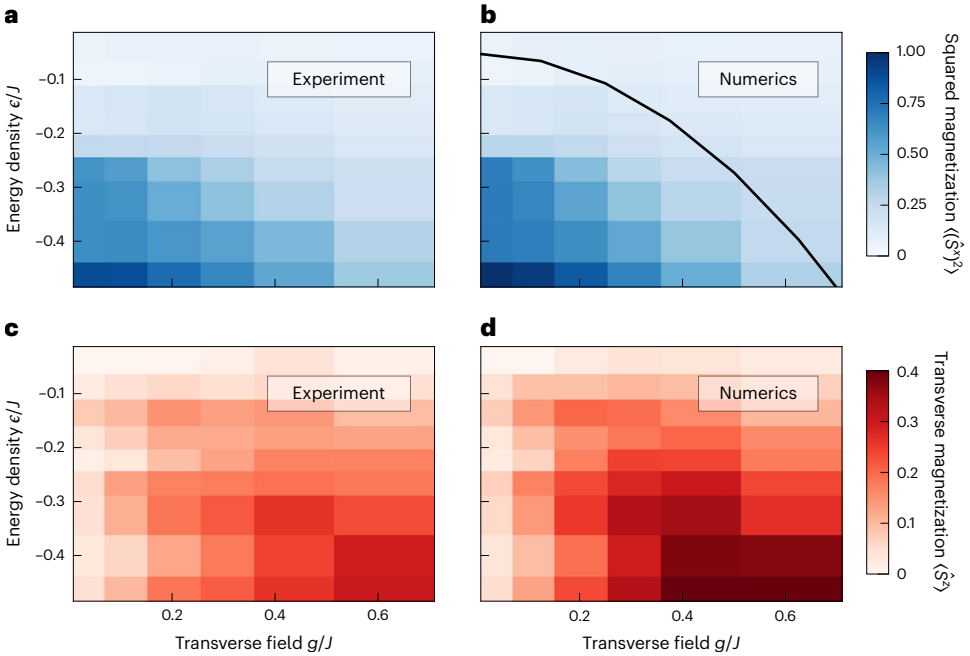

Fig. 3 | Equilibrium phase diagram. The probed region corresponds to the gold frame in Fig. 1c. **a**, Experimental squared magnetization. **b**, Numerical squared magnetization. **c**, Experimental transverse magnetization. **d**, Numerical transverse magnetization. Numerics are obtained by evolving to the same time as the experiment. $L = 13$. The transverse fields are $g/J = 0.04, 0.10, 0.21, 0.31, 0.41$ and 0.62. The black line is the phase transition line from Fig. 1c.

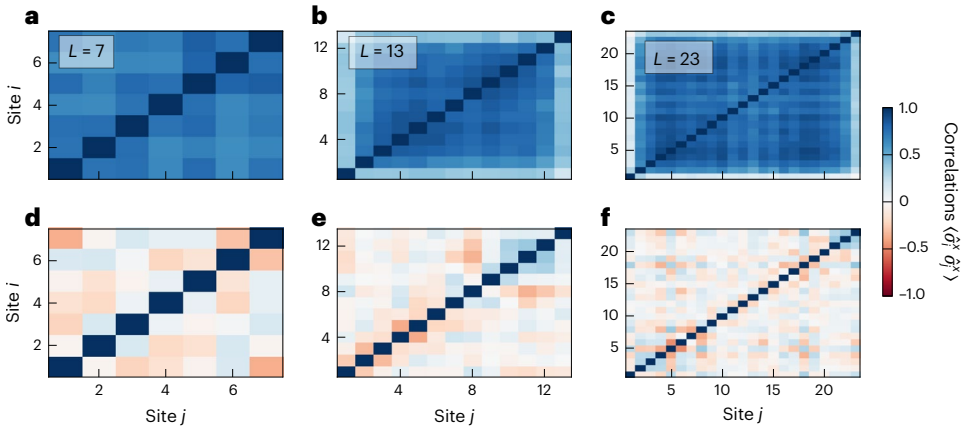

Fig. 4 | Correlations. Experimentally measured correlations at late times (not time averaged). **a**–**c**, Low energy ($\epsilon/J \approx -0.43$ (**a**), −0.46 (**b**) and −0.48 (**c**)). **d**–**f**, High energy ($\epsilon/J \approx 0$, −0.04 and 0.04) for $L = 7, g/J = 0.24$ (**d**), $L = 13, g/J = 0.31$ (**e**), and $L = 23, g/J = 0.18$ (**f**). Times are $Jt \approx 6.3, 10.2$ and 8.2 for $L = 7, 13$ and 23, respectively. For the corresponding numerical result, see Extended Data Fig. 6. The initial states are listed in Extended Data Table 1.

Observing a finite-energy phase transition

Having validated our scheme to prepare equilibrium states, we now use it as a tool to probe the phase diagram in Fig. 1c by repeating the procedure for many values of the magnetic field g/J. We display the result for the squared magnetization in Fig. 3a along with the numerical result, which was obtained by time evolving the initial states to the same time as the experiment. We find good agreement between the two. At low energy densities and small transverse fields, a large squared magnetization is observed. Conversely, at high energy densities and large transverse fields, the squared magnetization is small. This is consistent with a phase transition between a ferromagnet and an paramagnetic state. In particular, we find a good qualitative match between our finite-size experiment and the infinite-system-size extrapolation displayed in the gold frame in Fig. 1c, including in particular the phase transition line (Fig. 3b, black line). This indicates weak finite-size effects. More specifically, we also measured the squared magnetization for varying system sizes, indeed finding a qualitative match between them, with some residual finite-size dependence due to the slightly differing transverse field g/J and the inhomogeneity of the experimentally realized interactions (Methods and Extended Data Fig. 5).

To probe this transition further, we also measure the transverse magnetization, shown in Fig. 3c,d, again finding reasonable agreement between numerics and experiment. Importantly, we find a large transverse magnetization for large transverse fields and low energies, indicating a polarized state along the transverse field. This polarization is destroyed as we move to higher energy densities, which is indicative of a finite-energy crossover from a polarized paramagnet in the ground state at large transverse fields to an unpolarized state at high energies. The presence of this crossover results from the fact that, for large transverse field g/J, the energy density is proportional to the transverse

magnetization such that $\langle \hat{S}^z \rangle \to 0$ for $(\epsilon/J) \to 0$. In other words, the single-site reduced density matrix crosses over from a pure product state at low energies to an effective completely mixed state at high energies.

Counterintuitively, for intermediate energy scales around $\epsilon/J \approx -0.3$, the transverse magnetization displays a maximum as the field is increased and then decreases again as the field is increased further. This is due to the fact that our initial states have energy densities $\epsilon/J \lesssim 1/2$ (Fig. 1c, gold frame) while the ground-state energy decreases with g. This means that, as the transverse field is increased, we probe higher energy densities relative to the ground-state energy, explaining the decrease of the transverse magnetization.

Ordered phases are accompanied by long-range correlations throughout the system. We measured $\langle \hat{o}_i^x \hat{o}_j^x \rangle$ for three different system sizes at the lowest and highest energy densities (Fig. 4). We again find good agreement with numerical simulations (Extended Data Fig. 6). We find large positive correlations in the bulk of the system for low energies, confirming the presence of a ferromagnetically ordered state. At high energies, the correlations approximately vanish throughout the system, showing that the high-energy state is disordered. The fact that we find no substantial decay of the long-range correlations as we increase the system size is consistent with an existence of a ferromagnetic phase in the infinite system-size limit (Methods and Extended Data Fig. 6).

Discussion and outlook

In this work, we have for the first time studied a finite-energy phase transition in one spatial dimension. To do so, we introduced a simple, yet powerful, scheme to prepare equilibrium states in a trapped-ion quantum simulator. This scheme uses product state preparation as well as time evolution under a many-body Hamiltonian, which are among the simplest tasks in quantum simulators. Even though, in principle, our algorithm could be used as a quantum-inspired classical algorithm by replacing the quantum simulator with a classical algorithm simulating time evolution, this would be challenging in practice for large systems due to the reliance on non-equilibrium time evolution whose evaluation with classical methods is inefficient for the timescales necessary for thermalization.

We verified thermal state preparation by comparison with classical numerics. Outside of the regime of classical simulability verification could by achieved by using the fact that late-time expectation value of observables between different initial states with the same energy should agree in equilibrium. Fluctuation–dissipation relations measured by two-time correlation functions[42,43] could be used as a more rigorous indicator of thermalization, which would also yield the effective temperature. Finally, thermalization times could be reduced by weakly coupling engineered baths to the closed system evolution; this would also be accompanied by performance guarantees due to rigorous proofs of fast thermalization[44].

Our scheme can be immediately applied in a variety of analogue and digital spin-simulator platforms including Rydberg atoms, quantum dots and ultracold polar molecules to probe equilibrium states. For instance, equilibrium phases with continuous symmetry breaking[16,17,45] and other phases of various spin models[10,46] could be studied. In the future, the capability of quantum simulators to prepare different system sizes could be used for a finite-size scaling analysis to study finite-energy phase transitions more quantitatively. Furthermore, long-standing questions in condensed matter physics such as the nature of the excitations above spin-liquid ground states[47,48] could be studied in quantum simulators with our technique. In particular, dynamical correlation functions can be straightforwardly measured by using Ramsey interferometry[49,50].

Online content

Any methods, additional references, Nature Portfolio reporting summaries, source data, extended data, supplementary information, acknowledgements, peer review information; details of author contributions and competing interests; and statements of data and code availability are available at https://doi.org/10.1038/s41567-024-02751-2.

References

1. Kibble, T. W. B. Topology of cosmic domains and strings. *J. Phys. A* **9**, 1387 (1976).
2. Zurek, W. H. Cosmological experiments in superfluid helium? *Nature* **317**, 505–508 (1985).
3. Fukushima, K. & Hatsuda, T. The phase diagram of dense QCD. *Rep. Prog. Phys.* **74**, 014001 (2010).
4. Keimer, B., Kivelson, S. A., Norman, M. R., Uchida, S. & Zaanen, J. From quantum matter to high-temperature superconductivity in copper oxides. *Nature* **518**, 179–186 (2015).
5. Zinn-Justin, J. *Quantum Field Theory and Critical Phenomena* (Oxford Univ. Press, 2002).
6. van Hove, L. Sur l'intégrale de configuration pour les systèmes de particules à une dimension. *Physica* **16**, 137 (1950).
7. Landau, L. & Lifshitz, E. *Statistical Physics* (Butterworth-Heinemann, 1980); https://doi.org/10.1016/c2009-0-24487-4
8. Dyson, F. J. Existence of a phase-transition in a one-dimensional Ising ferromagnet. *Commun. Math. Phys.* **12**, 91 (1969).
9. Thouless, D. J. Long-range order in one-dimensional Ising systems. *Phys. Rev.* **187**, 732 (1969).
10. Defenu, N. et al. Long-range interacting quantum systems. *Rev. Mod. Phys.* **95**, 035002 (2023).
11. Jurcevic, P. et al. Quasiparticle engineering and entanglement propagation in a quantum many-body system. *Nature* **511**, 202–205 (2014).
12. Jurcevic, P. et al. Direct observation of dynamical quantum phase transitions in an interacting many-body system. *Phys. Rev. Lett.* **119**, 080501 (2017).
13. Zhang, J. et al. Observation of a many-body dynamical phase transition with a 53-qubit quantum simulator. *Nature* **551**, 601–604 (2017).
14. Zhang, J. et al. Observation of a discrete time crystal. *Nature* **543**, 217–220 (2017).
15. Choi, S. et al. Observation of discrete time-crystalline order in a disordered dipolar many-body system. *Nature* **543**, 221–225 (2017).
16. Feng, L. et al. Continuous symmetry breaking in a trapped-ion spin chain. *Nature* **623**, 713–717 (2023).
17. Chen, C. et al. Continuous symmetry breaking in a two-dimensional Rydberg array. *Nature* **616**, 691–695 (2023).
18. Tanzi, L. et al. Observation of a dipolar quantum gas with metastable supersolid properties. *Phys. Rev. Lett.* **122**, 130405 (2019).
19. Böttcher, F. et al. Transient supersolid properties in an array of dipolar quantum droplets. *Phys. Rev. X* **9**, 011051 (2019).
20. Joshi, M. K. et al. Observing emergent hydrodynamics in a long-range quantum magnet. *Science* **376**, 720 (2022).
21. Poulin, D. & Wocjan, P. Sampling from the thermal quantum gibbs state and evaluating partition functions with a quantum computer. *Phys. Rev. Lett.* **103**, 220502 (2009).
22. Temme, K., Osborne, T. J., Vollbrecht, K. G., Poulin, D. & Verstraete, F. Quantum Metropolis sampling. *Nature* **471**, 87–90 (2011).
23. Chowdhury, A. N. & Somma, R. D. Quantum algorithms for Gibbs sampling and hitting-time estimation. *Quantum Inf. Comput.* **17**, 41 (2017).
24. Motta, M. et al. Determining eigenstates and thermal states on a quantum computer using quantum imaginary time evolution. *Nat. Phys.* **16**, 205–210 (2019).
25. Zhu, D. et al. Generation of thermofield double states and critical ground states with a quantum computer. *Proc. Natl Acad. Sci. USA* **117**, 25402 (2020).

26. Lu, S., Bañuls, M. C. & Cirac, J. I. Algorithms for quantum simulation at finite energies. *PRX Quantum* **2**, 020321 (2021).
27. Shtanko, O. & Movassagh, R. Preparing thermal states on noiseless and noisy programmable quantum processors. Preprint at https://arxiv.org/abs/2112.14688 (2023).
28. Tazhigulov, R. N. et al. Simulating models of challenging correlated molecules and materials on the Sycamore Quantum Processor. *PRX Quantum* **3**, 040318 (2022).
29. Schuckert, A., Bohrdt, A., Crane, E. & Knap, M. Probing finite-temperature observables in quantum simulators of spin systems with short-time dynamics. *Phys. Rev. B* **107**, L140410 (2023).
30. Hémery, K. et al. Measuring the Loschmidt amplitude for finite-energy properties of the Fermi–Hubbard model on an ion-trap quantum computer. *PRX Quantum* **5**, 030323 (2024).
31. Srednicki, M. Thermal fluctuations in quantized chaotic systems. *J. Phys. A* **29**, L75 (1996).
32. Rigol, M., Dunjko, V. & Olshanii, M. Thermalization and its mechanism for generic isolated quantum systems. *Nature* **452**, 854–858 (2008).
33. Trotzky, S. et al. Probing the relaxation towards equilibrium in an isolated strongly correlated one-dimensional bose gas. *Nat. Phys.* **8**, 325–330 (2012).
34. Kaufman, A. M. et al. Quantum thermalization through entanglement in an isolated many-body system. *Science* **353**, 794 (2016).
35. Ghanem, K., Schuckert, A. & Dreyer, H. Robust extraction of thermal observables from state sampling and real-time dynamics on quantum computers. *Quantum* **7**, 1163 (2023).
36. Irmejs, R., Bañuls, M. C. & Cirac, J. I. Efficient quantum algorithm for filtering product states. *Quantum* **8**, 1389 (2024).
37. Reimann, P. Typical fast thermalization processes in closed many-body systems. *Nat. Commun.* **7**, 10821 (2016).
38. Katz, O., Feng, L., Risinger, A., Monroe, C. & Cetina, M. Demonstration of three- and four-body interactions between trapped-ion spins. *Nat. Phys.* **19**, 1452–1458 (2023).
39. Porras, D. & Cirac, J. I. Effective quantum spin systems with trapped ions. *Phys. Rev. Lett.* **92**, 207901 (2004).
40. Monroe, C. et al. Programmable quantum simulations of spin systems with trapped ions. *Rev. Mod. Phys.* **93**, 025001 (2021).
41. Kac, M., Uhlenbeck, G. E. & Hemmer, P. C. On the van der Waals theory of the vapor-liquid equilibrium. I. Discussion of a one-dimensional model. *J. Math. Phys.* **4**, 216 (1963).
42. Hartke, T., Oreg, B., Jia, N. & Zwierlein, M. Doublon-hole correlations and fluctuation thermometry in a Fermi–Hubbard gas. *Phys. Rev. Lett.* **125**, 113601 (2020).
43. Schuckert, A. & Knap, M. Probing eigenstate thermalization in quantum simulators via fluctuation-dissipation relations. *Phys. Rev. Res.* **2**, 043315 (2020).
44. Chen, C.-F. & Brandão, F. G. S. L. Fast thermalization from the eigenstate thermalization hypothesis. Preprint at https://arxiv.org/abs/2112.07646 (2023).
45. Yang, Y. et al. Simulating prethermalization using near-term quantum computers. *PRX Quantum* **4**, 030320 (2023).
46. Gong, Z.-X. et al. Kaleidoscope of quantum phases in a long-range interacting spin-1 chain. *Phys. Rev. B* **93**, 205115 (2016).
47. Semeghini, G. et al. Probing topological spin liquids on a programmable quantum simulator. *Science* **374**, 1242 (2021).
48. Satzinger, K. J. et al. Realizing topologically ordered states on a quantum processor. *Science* **374**, 1237 (2021).
49. Knap, M. et al. Probing real-space and time-resolved correlation functions with many-body Ramsey interferometry. *Phys. Rev. Lett.* **111**, 147205 (2013).
50. Schuckert, A. & Knap, M. Many-body chaos near a thermal phase transition. *SciPost Phys.* **7**, 022 (2019).

Methods

Experimental details

In this section, we introduce the trapped-ion experiment in more detail, specifically emphasizing how we prepare the interactions in equation (1) of the main text and how we choose the initial states.

Generating spin–spin interactions between ions. We induce spin–spin interactions among trapped ions through Raman transitions that virtually excite the collective motion of the ions. These Raman transitions are generated using pairs of beams: one that globally addresses the ion chain and another that individually targets each ion. The global addressing beam passes through an acousto-optical modulator (AOM) concurrently driven by two radio-frequency (RF) signals. This process splits the optical beam into two components, each with a distinct tone and nearly equal power, which are then projected onto the ion crystal. Simultaneously, a perpendicular array of tightly focused beams is directed toward the ion positions. Precise control of the trapping potential ensures a high degree of overlap between each ion and these beams. We achieve simultaneous and independent control over the amplitudes and frequencies of these beams using a multi-channel AOM. This configuration drives both the first red- and blue-sideband transitions within the dispersive regime. The beatnote frequencies for these transitions are detuned by $\pm(\omega_N + \Delta_\pm)$ from the carrier transition, where ω_N is the lowest frequency of the phonon mode along the radial direction. The detunings are nearly symmetric $|\Delta_+ - \Delta_-| \ll |\Delta_\pm|$.

This configuration generates the Hamiltonian in equation (1) for a chain of N ions. The asymmetry in the detunings between the two tones leads to an effective transverse magnetic field with an amplitude $g = (\Delta_+ - \Delta_-)/4$ in the frame that rotates at the carrier frequency. The symmetric part, $\Delta = (\Delta_+ + \Delta_-)/2$, corresponds to the average detuning of the effective spin-dependent force. This, in turn, generates the Ising Hamiltonian $\hat{H} = -\frac{1}{2\mathcal{N}}\sum_{i<j} J_{ij}\hat{\sigma}_i^x\hat{\sigma}_j^x$ with $\mathcal{N} = \frac{1}{L-1}\sum_{i<j}(J_{ij}/J)$ and an interaction matrix[16,40]

$$J_{ij} = \sum_k \frac{\eta_{ik}\eta_{jk}\Omega_i\Omega_j}{2(\Delta + \omega_N - \omega_k)}. \tag{S1}$$

Here, $\eta_{ik} = 0.08 b_{ik}$ are the Lamb–Dicke parameters, with b_{ik} as the mode participation matrix elements describing the coupling between spin i and motional mode k (ref. 38). Ω_i denotes the equivalent resonant carrier Rabi frequency at ion $1 \le i \le N$ for each tone, and ω_k represents the motional frequencies along one radial direction in the y–z plane (labelled in decreasing order with $1 \le k \le N$). These frequencies are determined by the trapping potential; we use a quadratic trapping potential in the radial direction with centre-of-mass frequency of $\omega_1 = 2\pi \times 3.075$ MHz and an axial electrostatic potential of $V(x) = c_4x^4 + c_2x^2$, where $c_2 = 0.11$ eV mm^{-2} and $c_4 = 1.6 \times 10^3$ eV mm^{-4} for a 15-ion chain and $c_2 = -0.1$ eV mm^{-2} and $c_4 = 235$ eV mm^{-4} for a 27-ion chain. Here, x is the coordinate along the chain axis. These potentials result in a nearly uniform spacing of the central ions in the crystal, except for the edges, with a spacing of 3.75 μm to match the centres of the uniformly spaced beams used for individual addressing. The motion of the ions in the y–z (radial) plane is described by two sets of N collective phonon modes, representing the ions' motion along two orthogonal directions. The effective wave vector of the optical field is spatially aligned to selectively drive a single set of these radial phonon modes in the y–z plane. The effective wave vector of the optical field is aligned to selectively drive only one specific set of radial phonon modes.

To estimate the form of the J_{ij}, we calculate the mode participation factors by solving the Laplace equation assuming harmonic radial potential with a strength measured from experiment and used the electrode voltages, from which we find the positions of the ions, from which we determine the mode participation matrix elements and the eigenfrequencies. This then enables us to calculate the $\tilde{J}_{ij}$ from the measured individual Rabi frequencies and the detunings from the modes using equation (S1); see ref. 16 for more details on our setup.

We detune Δ to the red side of the mode spectrum ($\Delta < 0$) to primarily couple to phonon modes characterized by rapidly varying mode participation factors (that is, near the zig-zag phonon mode and far from the centre-of-mass phonon mode). For a uniform-spaced ion chain, this choice results in an interaction matrix $\tilde{J}_{ij}$ consisting of two terms primarily dependent on the ion separation distance $|i-j|$: an inverse cubic (power-law) term and an exponentially decreasing term that alternates with the spin distance, appended by a factor $(-1)^{|i-j|}$. As we reduce $|\Delta|$, the exponential term becomes dominant over the power-law term, particularly at short distances. To generate a non-alternating $\tilde{J}_{ij}$ matrix, we shift the optical phase of the individual beam array in a staggered way, shifting the phase of all odd beams by π.

Individual control over the beam amplitudes provides additional flexibility in manipulating the interaction matrix. Specifically, by turning off the beam targeting ion q, we effectively eliminate J_{qi} for all $1 \le i \le N$, rendering its participation in the phonon modes independent of its spin. This capability allows us to simulate the evolution of $L \le N$ spins in an N-ion chain. Utilizing this technique, we realize the interaction of $L = 7$, 13 and 23 spins in chains of $N = 15$, 15 and 27 ions, respectively, with the beams symmetrically turned off near the crystal's edges. Not including the edge ions' spins allows us to achieve chains with more uniform spacing through the presence of their charge.

For the $L = 7$ and 13 configurations, we use uniform beam amplitudes. In the case of the $L = 23$ configuration, the relative Rabi frequencies of the 23 beams are chosen as follows: [1, 1, 0.72, 0.76, 0.6, 0.72, 0.63, 0.81, 0.72, 0.91, 0.78, 0.94, 0.78, 0.9, 0.72, 0.8, 0.62, 0.71, 0.59, 0.75, 0.71, 0.99, 1], alleviating the variation of the interaction strength across the chain due to the spatial dependence of the rapidly varying mode participation factors. We define $J = 2\max_{ij}(J_{ij})$ and had $J \approx 2 \times 2\pi$ kHz in all experiments. The detunings are set at $\Delta = -2\pi \times 100$ kHz for $L = 7$, $\Delta = -2\pi \times 35$ kHz for $L = 13$ and $\Delta = -2\pi \times 9$ kHz for $L = 23$.

To account for the light shift induced by the beams on the ions in each configuration, we perform calibration and compensation by applying an opposite shift to the optical frequencies of the individual beams. For the $L = 13$ configuration, we additionally use a variation of a dynamical decoupling technique[51] that we have found effective in mitigating σ_z noise (such as light-shift noise). In particular, we break the Hamiltonian evolution into two periods, separated by a short π pulse that is applied to all spins, rotating around the x axis. Inverting the sign of g for the second evolution period yields the same evolution as the original Hamiltonian.

Initial-state preparation. The initial states are chosen by selecting target energies E_{target} equally spaced in a window $[E_{\min}, E_{\max}]$, where $E_{\min}$ is the energy of the totally polarized state (that is, the ground state for $g = 0$) and $E_{\max}$ is some high-energy limit close to zero. We then find the x-product state $|\psi\rangle$ which minimizes $|\langle\psi|\hat{H}|\psi\rangle - E_{\text{target}}|$ for all E_{target}, using the experimental J_{ij}. In practice, we do this by calculating $\langle\psi|\hat{H}|\psi\rangle$ for all 2^L states $|\psi\rangle$, which is numerically cheap even for $L = 23$. For much larger systems, finding states closest to a particular energy could be done by using an optimization algorithm. We show the thus selected initial states in Extended Data Table 1. Note that states with the same number of spin flips can have different energies due to the lack of translational invariance and the inhomogeneities present in the experimentally realized J_{ij} (Extended Data Fig. 1).

The preparation of product states begins with optical pumping, initially aligning all spins to the $\downarrow_z$ state by coupling the spin states in the $F = 1$ manifold of the ground state to the $^2P_{1/2}$ levels. A repump at 935 nm is used to depopulate any leakage to the $^2D_{3/2}$ state. Subsequently, spins are rotated by simultaneously applying short (~1 μs) single-qubit rotation pulses to all spins in the chain. This operation rotates the ith

spin by polar angle θ_i and azimuthal angle ϕ_i via the rotation operator $R(\theta_i, \phi_i)$. We achieve this operation using Raman beams to drive the carrier transition and set $\theta_i = \pi/2$ for all ions by adjusting the power of the individual beams, which are independently calibrated to account for any inhomogeneity in the ions' positions and non-uniformity of the global beam. To set the spin orientation of the initial spin state in the x basis, we set the optical phase of the ith beam in the array as $\phi_i = \pi/2$ ($\phi_i = 3\pi/2$) if the initial state corresponds to $\uparrow$ ($\downarrow$), with the quantization axis along x. The ability to simultaneously shift the phase of each optical beam in the array is enabled by local parallel RF control on our multi-channel AOM.

To test the experimental preparation of these initial states, we evaluate the energy from measurements of $\langle\hat{\sigma}_i^x\hat{\sigma}_j^x\rangle$, $\langle\hat{\sigma}_i^z\rangle$ as well as the calculated J_{ij} in equation (S1) and the experimentally calibrated value of g/J. We show the results of these measurements for $L = 13$ in Extended Data Fig. 2 for different g/J. These measurements are in good agreement with the theoretical calculation, which confirms that the J_{ij} are as we expect them to be and that initial-state preparation is good. In particular, the energy does not strongly depend on g/J, which confirms that there is no substantial component of the initial state in the direction of the transverse field. We also find reasonable conservation of the energy as a function of time, providing a measure for the strength of decoherence processes in our simulator. We further study the influence of decoherence on the dynamics in the next section.

As visible in Fig. 3 of the main text, we found less good agreement between theory and experiment for the transverse magnetization than for the squared magnetization. We attribute at least some of this additional error to over-underrotation errors in the state preparation. Indeed, we observed that the initial transverse magnetization is not exactly vanishing (Extended Data Fig. 3a). To test this hypothesis further, we used numerical simulations in which we slightly rotated the initial product state around the y axis to reproduce the experimentally measured transverse magnetization (Extended Data Fig. 3b), finding better agreement with the experiment than with initial states purely along the x direction.

Influence of errors on the dynamics. Unitary spin evolution is accompanied by noise, which we associate with three dominant processes. One noise process stems from a noisy spin-dependent shift, associated with $\hat{\sigma}_i^z$ as the jump operator, originating primarily from fluctuations in the a.c. light shift associated with the Raman drive. Therefore, for a nearly uniform beam drive, the noise is approximately common mode and the jump operator is $\sum_{i=1}^{N}\hat{\sigma}_i^z$. The second noise process is related to spin-flip errors associated with the jump operator $\hat{\sigma}_i^x$, which originates from off-resonant spin excitation correlated with phonon transitions. However, owing to the detuning of the drive from the phonon mode spectrum, this coupling oscillates at a timescale much faster than the spin–spin dynamics, so the error manifests itself as a time-constant error, which, to lowest order, affects only state preparation. The third process pertains to shot-to-shot variations in the strength of the J_{ij} coefficients owing to effective noise in the drive strength Ω_i that is prominent for long chains of ions[52]. To show that all of these noise processes do not have a substantial influence on the dynamics, we estimate their strength experimentally using independent calibration experiments and then classically simulate the full many-body dynamics in the presence of the noise, to further validate the agreement of the experiment with the noiseless numerics presented in the main text.

We estimate the strength of the dephasing process due to the a.c. Stark shift by initializing the system in state $|\uparrow\cdots\uparrow\rangle$ and applying the $g = 0$ Hamiltonian. We fit the measured magnetization as a function of time to an exponential fit function $\frac{1}{L}\sum_i\langle\hat{\sigma}_i^x(t)\rangle = \exp(-\gamma t)$ using the dephasing rate $\gamma \approx 4\times10^{-3}J$ as a single fitting parameter. We simulate the dephasing process in our numerics by applying on g a white noise whose variance yields the same measured decay[53].

The strength of the spin-flip state-preparation errors is estimated by preparing pairs of neighbouring spins in state $|\downarrow\uparrow\rangle_z$ and applying a single pair of Raman beams that drives their Ising coupling, that is the Hamiltonian $\frac{J}{2}\hat{\sigma}_i^x\hat{\sigma}_{i+1}^x$ with no transverse field. We then measure the parity-related observable $\langle\hat{\sigma}_i^z\hat{\sigma}_{i+1}^z\rangle$, which should be −1 in the absence of errors. We find this observable to be approximately independent of time, confirming the time-constant nature of the error. Modelling this error as a single-spin bit-flip process, we extract its probability p per ion via $p = \frac{1}{2}(1-\sqrt{-\langle\hat{\sigma}_i^z\hat{\sigma}_{i+1}^z\rangle})$, assuming $p < 0.5$ and, therefore, $\langle\hat{\sigma}_i^z\hat{\sigma}_{i+1}^z\rangle < 0$. From these calibration measurements, we find p_i = [0.08, 0.1, 0.13, 0.16, 0.16, 0.15, 0.14, 0.15, 0.16, 0.17, 0.17, 0.13, 0.1] for our 13-ion chain. In our numerical simulations, we include this error by flipping the spin i with probability p_i before we start the dynamics.

Finally, we estimate the shot-to-shot variation of the J_{ij} using the same experimental procedure as the spin-flip state preparation errors by extracting $(\langle\hat{\sigma}_{i+1}^z\rangle - \langle\hat{\sigma}_i^z\rangle)/(\langle\hat{\sigma}_{i+1}^z\rangle + \langle\hat{\sigma}_i^z\rangle)$ and fitting a function $\exp(-(Jt)^2/(2\sigma^2))\cos(Jt)$. The denominator divides out single-qubit errors, which are primarily caused by dephasing between the two opposite spin states spanning the −1 parity. The fitting function is obtained by assuming shot-to-shot fluctuations of the form $J \to J(1+\delta)$, where δ are Gaussian distributed with mean zero and variance $1/\sigma^2$, which is a good model at short times[52]. We find σ between 0.07 and 0.14 over the 12 bonds in the chain. In our numerics, we assume that the shot-to-shot variations are perfectly spatially correlated, that is, $J_{ij} \to J_{ij}(1+\delta)$ and take $\sigma = 0.14$, providing an upper bound on the experimentally measured noise.

We show the result of the simulations including all three sources of noise in Extended Data Fig. 3c,d. In general, we find that the noise does not alter the dynamics substantially. The largest visible difference between the noisy results and the noiseless results is in the dynamics of $\langle(\hat{S}^x)^2\rangle$ for the totally polarized state at the smallest magnetic field, where the a.c. Stark shift dephasing leads to a small but visible decay of the signal.

We also estimated the accuracy with which we set the transverse field g in a dedicated calibration experiment. We measure g by evolving a spin state, initially prepared in $|\uparrow\cdots\uparrow\rangle$, under the Ising Hamiltonian for various values of g near zero. We measured magnetization $\langle\hat{\sigma}_i^x\rangle(g)$ and found a quadratic dependence on g, with the value of g that resulted in the average (over i) smallest magnetization indicating the actual zero transverse field, for which the spins do not evolve. Using this technique to estimate g, we can characterize how well we correct for slow errors, probably due to slow variations or drift in the light shift associated with the beams driving the Ising interaction. These drift errors are independent of the target value of g in the experiment because the latter depends on the frequency shift of the beams, which can be determined with high precision. To compensate for light-shift variations, we run two routine rapid calibrations: one adjusts the d.c. trapping potential minima to optimally align the ions with the Raman beams array, and the second adjusts the laser amplitude to maintain accurate reference single-qubit rotations. We typically run these calibrations every 20 min. Measuring the value of g after one such cycle shows that these calibrations maintain the g value relatively well; the measured value between two calibration cycles varied by 26 Hz, corresponding to an accuracy error of approximately 1% in units of J.

Equilibrium phase diagram

In this section, we determine the finite-temperature phase diagram of the model in equation (1) of the main text and discuss how to probe it in the finite-energy setting of the experiment.

Finite-temperature phase diagram. To extract the equilibrium properties of the model presented in the main text, we use matrix-product-state (MPS) simulations in the canonical ensemble using the purification algorithm[54,55] and the W_{II} matrix-product-operator time evolution method[56] implemented in the TeNPy library[57]. We choose

double-floating-point precision, a timestep of $\Delta t = 0.02$ and a bond dimension of 16, and checked that the absolute error in the observables was less than 1% compared with simulations with half the timestep and double the bond dimension. The error due to floating point precision is inconsequential in our simulation.

We use the standard procedure (see, for example, ref. 50) of using the Binder cumulant[58–60]

$$U_4 = 1 - \frac{\left\langle \left(\hat{S}^x\right)^4 \right\rangle}{3\left\langle \left(\hat{S}^x\right)^2 \right\rangle^2} \tag{S2}$$

to detect the ferromagnetic phase transition. In this expression, $\langle \hat{S}_x^2 \rangle \equiv \sum_{ij} \langle \hat{\sigma}_i^x \hat{\sigma}_j^x \rangle / L^2$, $\langle \hat{S}_x^4 \rangle \equiv \sum_{ijkl} \langle \hat{\sigma}_i^x \hat{\sigma}_j^x \sigma_k^x \sigma_l^x \rangle / L^4$. The Binder cumulant is equal to 2/3 (0) deep in the ferromagnetic (paramagnetic) phase, and the leading finite-size corrections cancel at the phase transition. Hence, calculating the Binder cumulant for consecutive system sizes, extracting their crossing points and extrapolating those to infinite system size leads to a precise estimate for the critical temperature. We show one such procedure in Extended Data Fig. 4a,b and a comparison of our MPS simulations with a classical Monte Carlo simulation for $g = 0$ in Extended Data Fig. 4c. We estimate an error of our extrapolation by comparing the critical temperature T_c obtained from system sizes 16, 32, 64 and 16, 32, 64, 128, finding an error of 0.01–0.03J.

We show the thus-extracted phase diagram in Extended Data Fig. 4d. For $\gamma = 0$ (infinite-range interactions), we find excellent agreement with the mean-field solution $T_c/J = (g/J)/\mathrm{arctanh}(g/J)$. Interestingly, we find that T_c/J increases as γ/J is increased. This indicates that the model shows a phase transition even for large γ/J. For large γ, however, increasingly large system sizes are needed to capture the phase transition, which limits the range of our simulations. For $g/J = 1$, we find Binder cumulant crossing points that move towards higher temperature as the system size is increased. This indicates that the model is paramagnetic for $g/J > 1$ for all γ studied here.

Scaling. We also extract one of the critical exponents from the Binder cumulant by using the method described for example in ref. 61: we fit $T_c(L) = T_c(1 + aL^{-\omega-\theta_t})$ to the crossing temperatures and $U_{4,c}(L) = b + cL^{-\omega}$ to the values of the Binder cumulant at the crossing temperatures, where b and c are real fitting constants. From this, we can extract θ_t, which is connected to the critical exponent ν and find $\theta_t \approx 0.5$, 0.52, 0.54 and 0.69 for $g = 0.0$, 0.25, 0.5 and 0.75. Surprisingly, this indicates a dependence of θ_t on the transverse field. However, we emphasize that our estimates are rather low-confidence because of the comparatively small system sizes used here. Moreover, we cannot give error estimates for y_t because we use three data points to fit three parameters. Nevertheless, we show that the thus-found θ_t leads to a good scaling collapse of the Binder cumulant (see Extended Data Fig. 4e and compare with Extended Data Fig. 4a for the uncollapsed data). The exponent $\theta_t = 0.5$ corresponds to the mean-field exponent, which is exact in the all-to-all connected model $\gamma = 0$. We also extract a slightly different T_c from this procedure but generally find agreement with the procedure shown in Extended Data Fig. 4a,b within about 3%.

Energy phase diagram from canonical simulations. We extract the finite-energy/microcanonical properties of the model by using the equivalence of ensembles in the infinite-system-size limit. To do so, we extrapolate the energy as a function of temperature $E(T)$ to infinite system size (Extended Data Fig. 4f). Doing the same for observables (Extended Data Fig. 4g) enables us to convert all observables to be as a function of energy instead of temperature by similarly extrapolating the value of the observables to infinite system size. In particular, we obtain the critical energy line shown in Fig. 1c of the main text by using the extrapolated numerically obtained $E(T)$ to obtain the critical energy E_c/J from the critical temperature T_c/J, which was obtained by the procedure discussed in 'Equilibrium phase diagram' section.

Finite-size effects in energy-dependent observables. The finite-size dependence of temperature-dependent observables in the vicinity of the critical temperature of a second-order phase transition can be captured by considering the growth of the correlation length as the system size increases, leading to the theory of finite-size scaling. However, much less is known about finite-size scaling in the microcanonical ensemble[62] and even less in the diagonal ensemble, which is the one experimentally realized in this work. To get a rough idea for how strong finite-size effects are on energy-dependent observables, we display the squared magnetization for different system sizes as a function of energy, evaluated with MPS simulations in the canonical ensemble in Extended Data Fig. 4h. We find that the finite-size corrections for $L \gtrsim 32$ are almost invisible for this observable and much weaker than, for instance, the finite-size corrections in the Binder cumulant as a function of temperature shown in Extended Data Fig. 4a. This is in tune with the observation that the measured squared magnetization for $L = 13$ shown in Fig. 3 of the main text is close to the infinite-system-size extrapolation shown in Fig. 1c. We found that finite-size effects become stronger as g/J is increased. Moreover, we find in Extended Data Fig. 4h that the squared magnetization extrapolated to infinite system size does not exactly vanish at the critical energy extracted from evaluating the infinite-system-size extrapolated energy at the critical temperature. We attribute this to the fact that the infinite-system-size extrapolation has not fully converged yet for both the critical energy (c.f. the grey error bar lines in Extended Data Fig. 4h) and also the squared magnetization in the vicinity of the critical energy (c.f. the uncertainty for both the energy density and the squared magnetization in Extended Data Fig. 4f,g). We note that this is to be expected for finite-size extrapolation of the order parameter in an Ising-like transition as in a finite-size system the order parameter rounds off, leading to a small but non-vanishing magnetization even for $\epsilon/J > \epsilon_c/J$ in finite systems, where ϵ_c is the critical energy density.

To test how experimental imperfections in the interactions due to inhomogeneities affect this result, we compare the canonical result using the calculated experimentally realized interactions (c.f. Extended Data Fig. 1) with the corresponding result using the ideal, homogeneous interactions. We find that the inhomogeneities in the interactions lead to deviations from the homogeneous result, which hampers a systematic finite-size extrapolation. Nevertheless, as shown in Extended Data Fig. 5, the experimental data, which are data obtained from time evolution, show little finite-size effects as expected from our numerical calculations for homogeneous interactions. Moreover, we note that, in principle, the interactions could be made homogeneous by further engineering the addressing beams[63]. We attribute the main source of the deviation of the experimental data from the noiseless numerics to the systematic error coming from the fact that we evolved only to finite times.

Correlation functions. In Extended Data Fig. 6, we show numerically calculated correlation functions at high and low energy with the same parameters as in Fig. 4. We evolved to the same time as in the experiment and used the calculated experimentally realized interactions shown in Extended Data Fig. 1. We find, in general, good agreement. In particular, the remnant of ferromagnetic correlations in the top right corner of Extended Data Fig. 6b, $L = 13$ and $L = 23$, is also visible in the experimental result, showcasing that the measured patterns are indeed physical. Moreover, the slight reduction in correlations in the centre of Extended Data Fig. 6a, $L = 23$, is also visible in the experiment, albeit is less pronounced.

To show the crucial role of normalizing the exponent of the exponential decay of the interactions by $1/L$, we show in Extended Data Fig. 6c,d the correlation function $\langle \hat{\sigma}_i^x \sigma_j^x \rangle$ for the definition of the

Hamiltonian in the main text (that is, with perfectly homogeneous interactions) as well as without the normalization, that is,

$$J_{ij}^{\text{unnormalized}} = \exp\left(-\frac{\gamma}{13}|i-j|\right), \tag{S3}$$

with $\gamma = 10.8$, where we chose the denominator to match the definitions for the relatively small system size $L = 13$. We find that, while the correlations become longer ranged as the system size increases for the definition in the main text, the correlations decay to zero quickly as the system size increases when using $J_{ij}^{\text{unnormalized}}$, showing the absence of a long-range-ordered phase at this temperature. This is in agreement with the expectation that purely exponentially decaying interactions are in the universality class of the model with nearest-neighbour interactions.

Time-evolution method to evaluating equilibrium observables

In this section, we introduce our method in greater detail and check several underlying assumptions for our specific case.

Overview of the method. Our method to experimentally prepare thermal states is using a measurement of time-averaged observables $\hat{O}$

$$\overline{\langle\psi|O(\hat{t})|\psi\rangle} \equiv \int_0^T \mathrm{d}t\langle\psi|O(\hat{t})|\psi\rangle \overset{T\to\infty}{\to} \sum_n |\langle n|\psi\rangle|^2\langle n|\hat{O}|n\rangle \tag{S4}$$

with respect to an initial state $|\psi\rangle$ of energy $E = \langle\psi|\hat{H}|\psi\rangle$. In the second step, we inserted the energy eigenbasis $\hat{H}|n\rangle = E_n|n\rangle$ and assumed that the Hamiltonian has a non-extensive number of degenerate states. The ETH[31] states that the expectation values of a local observable $\hat{O}$ with respect to eigenstates $|n\rangle$ of the Hamiltonian with eigenenergy E_n are given by

$$\langle n|\hat{O}|n\rangle = \mathcal{O}(E_n), \tag{S5}$$

where $\mathcal{O}(E_n)$ is the value of the observable in the microcanonical ensemble at energy E_n, which is a smooth function of energy. If the probability distribution $|\langle n|\psi\rangle|^2$ has a vanishing energy-density variance $(\langle\psi|\hat{H}^2|\psi\rangle - \langle\psi|\hat{H}|\psi\rangle^2)/L^2 \overset{L\to\infty}{\to} 0$ in the thermodynamic limit, then we can directly follow from ETH that $\sum_n|\langle n|\psi\rangle|^2\langle n|\hat{O}|n\rangle = \mathcal{O}(E)\sum_n|\langle n|\psi\rangle|^2 = \mathcal{O}(E)$ and, therefore,

$$\overline{\langle\psi|O(\hat{t})|\psi\rangle} \to \mathcal{O}\left(\langle\psi|\hat{H}|\psi\rangle\right). \tag{S6}$$

This motivates the following protocol to evaluate expectation values of observables in the microcanonical ensemble, which we follow in the main text:

(1) Prepare initial state $|\psi\rangle$, for example a product state, with energy $E_\psi = \langle\psi|\hat{H}|\psi\rangle$.
(2) Evolve under Hamiltonian $\hat{H}$ until time t.
(3) Measure $\hat{O}$ at various times $t \le T$.
(4) Evaluate the time average in equation (S4).
(5) Converge with respect to T.

Finite-size effects of the diagonal ensemble. For the diagonal ensemble expectation values (that is, the late-time expectation values of observables) to approach the microcanonical ensemble, the expectation values of the observables with respect to the eigenstates $\langle n|\hat{O}|n\rangle$ should form a smooth function of the energy E_n over the width of the diagonal ensemble $|\langle n|\psi\rangle|^2$. In a finite system, both of these conditions can be and often are violated. This means that the long-time expectation value of an observable evolved from two initial states that are close in energy can be very different. We show this observation for our system in Extended Data Fig. 7, where we show the diagonal ensemble expectation values along with the time-averaged expectation value of the observable evolved to the latest time available in the experiment for all 2^L x-product states, as well as the canonical ensemble and the experimental data. We find that, for small transverse fields, the scatter around the canonical ensemble is larger, which we attribute to the interplay between the weak breaking of integrability at $g = 0$ and finite-size effects. We also find that the time we evolved to in the experiment is largely long enough to reproduce the overall behaviour as a function of energy, with some finite-time differences visible for $g/J = 0.21$ and $L = 13$.

We also note that the states we chose in the experiment by the procedure described in 'Initial-state preparation' section are roughly representative of all states, that is, their scatter around the canonical ensemble is similar to the scatter of all product states.

Verification of thermalization. In Extended Data Fig. 8, we show the analogue of Fig. 2 in the main text across all transverse fields shown in Fig. 3 of the main text, with the same initial states for all fields, tabulated in Extended Data Table 1b. We find a similarly good match for all fields, with the agreement becoming better for larger fields. For the numerical calculations, we used the interactions shown in Extended Data Fig. 1b.

To test thermalization more rigorously, we perform MPS simulations for larger systems, starting from the totally polarized initial state $|\uparrow\cdots\uparrow\rangle$, defined along the x axis (that is, the lowest-energy product initial state for $g = 0$). We show the relative deviation from the thermal expectation value (obtained from purification-MPS simulations, as introduced in 'Finite-temperature phase diagram' section, at the same system size) in Extended Data Fig. 9. We find that, for small fields, the relative error reaches a plateau as a function of time, with the value of the plateau decreasing for increasing system size, which is an indication that, in the infinite-time and infinite-system-size limit, the long-time value and the thermal value approach each other. In general, the relative error increases with transverse field. At around $g/J \approx 0.625$, we find an approximately power-law decay of the relative error instead of a plateau, before erratic oscillations set in that depend heavily on the time step and bond dimension. For even larger fields, a plateau is again reached that, however, now tends to larger error as the system size is increased. This is to be expected as, for large transverse fields, this model shows prethermalization: instead of a thermalization to the transverse-field Ising model, the system thermalizes to the XY model owing to the quasi-conservation of the transverse field. Indeed, at large transverse field, the long-time value of the squared magnetization approaches 1/2 as expected from the XY model instead of 0 as expected from the transverse field Ising model. Moreover, at intermediately large field, this deviation from thermal behaviour has been associated to a dynamical quantum phase transition[13,64,65], but the exact relation to prethermalization is unresolved. In any case, these effects constrain the applicability range of our method to small values of the transverse field.

Data availability

All data are available from the corresponding authors upon reasonable request.

Code availability

All codes are available from the corresponding authors upon reasonable request.

References

51. Morong, W. et al. Engineering dynamically decoupled quantum simulations with trapped ions. *PRX Quantum* **4**, 010334 (2023).
52. Cetina, M. et al. Control of transverse motion for quantum gates on individually addressed atomic qubits. *PRX Quantum* **3**, 010334 (2022).

53. Gardiner, C. W. *Handbook of Stochastic Methods* (Springer, 2009).
54. Barthel, T. Matrix product purifications for canonical ensembles and quantum number distributions. *Phys. Rev. B* **94**, 115157 (2016).
55. Hauschild, J. et al. Finding purifications with minimal entanglement. *Phys. Rev. B* **98**, 235163 (2018).
56. Zaletel, M. P., Mong, R. S. K., Karrasch, C., Moore, J. E. & Pollmann, F. Time-evolving a matrix product state with long-ranged interactions. *Phys. Rev. B* **91**, 165112 (2015).
57. Hauschild, J. & Pollmann, F. Efficient numerical simulations with tensor networks: Tensor Network Python (TeNPy). *SciPost Phys. Lect. Notes* 5 (2018).
58. Binder, K. Finite size scaling analysis of ising model block distribution functions. *Z. Phys. B* **43**, 119–140 (1981).
59. Wolff, U. Collective Monte Carlo updating for spin systems. *Phys. Rev. Lett.* **62**, 361 (1989).
60. Luijten, E. & Blöte, H. W. Monte Carlo method for spin models with long-range interactions. *Int. J. Modern Phys. C* **6**, 359 (1995).
61. Lazo, E. G., Heyl, M., Dalmonte, M. & Angelone, A. Finite-temperature critical behavior of long-range quantum Ising models. *SciPost Phys.* **11**, 076 (2021).
62. Desai, R. C., Heermann, D. W. & Binder, K. Finite-size scaling in a microcanonical ensemble. *J. Stat. Phys.* **53**, 795 (1988).
63. Korenblit, S. et al. Quantum simulation of spin models on an arbitrary lattice with trapped ions. *New J. Phys.* **14**, 095024 (2012).
64. Halimeh, J. C. et al. Prethermalization and persistent order in the absence of a thermal phase transition. *Phys. Rev. B* **95**, 024302 (2017).
65. Žunkovič, B., Heyl, M., Knap, M. & Silva, A. Dynamical quantum phase transitions in spin chains with long-range interactions: merging different concepts of nonequilibrium criticality. *Phys. Rev. Lett.* **120**, 130601 (2018).

Acknowledgements

We acknowledge discussions with H. Dreyer, K. Ghanem, K. Hémery, M. D. Lukin and T. V. Zache. This material is based upon work supported by the US Department of Energy, Office of Science, National Quantum Information Science Research Centers, Quantum Systems Accelerator (DE-FOA-0002253). Additional support is acknowledged from the NSF STAQ Program (PHY-1818914) and the AFOSR MURI on Dissipative Quantum Control (FA9550-19-1-0399). A.S., E.C. and A.V.G. were also supported in part by the NSF QLCI (award no. OMA-2120757), the DoE ASCR Quantum Testbed Pathfinder program (award nos. DE-SC0019040 and DE-SC0024220), DoE ASCR Accelerated Research in Quantum Computing program (award no. DE-SC0020312), AFOSR, ARO MURI, AFOSR MURI and the DARPA SAVaNT ADVENT programme.

Author contributions

A.S. and O.K. devised the research. O.K., L.F., A.D. and C.M. contributed to the experimental setup. O.K. and L.F. performed experiments. A.S. performed numerical simulations. A.S., O.K. and L.F. analysed the experimental data. A.S., E.C., M.H. and A.V.G. contributed to the theoretical analysis. A.V.G. and C.M. supervised the research. A.S. wrote the initial paper, and all authors contributed revisions.

Competing interests

C.M. is a founder of IonQ, Inc. and has a personal financial interest in the company. The other authors declare no competing interests.

Additional information

Extended data is available for this paper at https://doi.org/10.1038/s41567-024-02751-2.

Correspondence and requests for materials should be addressed to Alexander Schuckert or Or Katz.

Peer review information *Nature Physics* thanks Alvise Bastianello, Manoj Joshi and the other, anonymous, reviewer(s) for their contribution to the peer review of this work.

https://doi.org/10.1038/s41567-024-02751-2

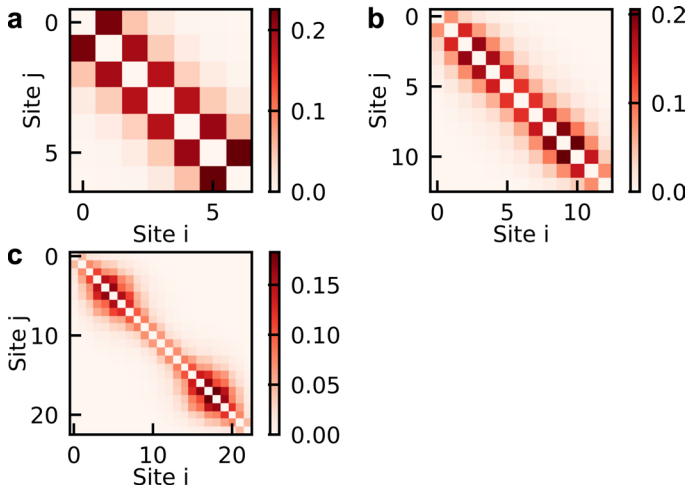

Extended Data Fig. 1 | Interaction matrices. Normalised experimentally realized interaction matrices $J_{ij}/(2JN)$ calculated from the mode spectrum and the beam parameters. **a**, L=7, **b**, L=13, **c**, L=23.

https://doi.org/10.1038/s41567-024-02751-2

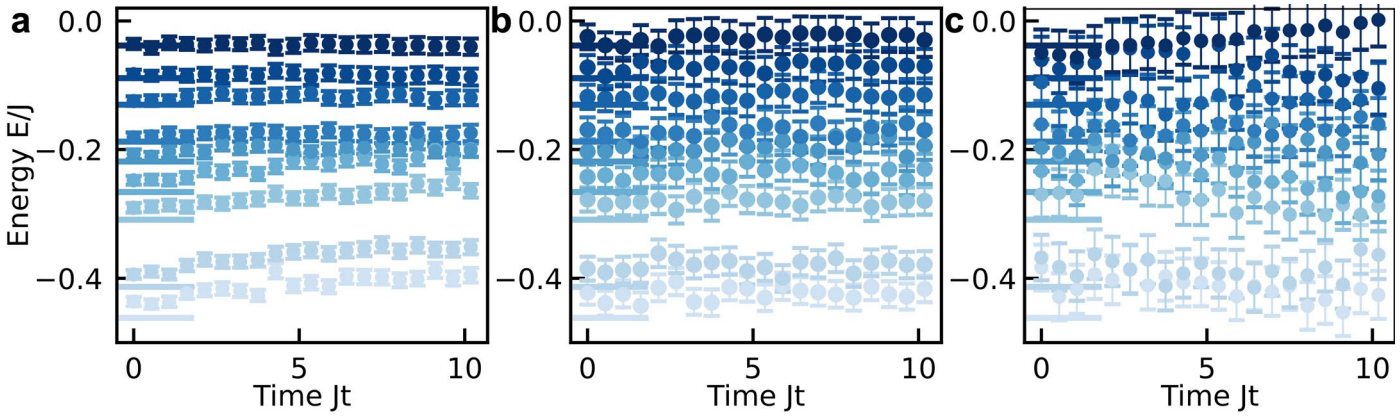

Extended Data Fig. 2 | Measured energies. Time evolution of the measured energy for three different fields and all initial states prepared in Fig. 2 of the main text. **a**, g/J=0.04, **b**, g/J=0.21, **c**, g/J=0.41. Errors from quantum projection noise for the spin observables and Gaussian error propagation. Error bars increase for larger *g*/*J* because the error bar is dominated by the transverse field term and is hence proportional to *g*/*J*. Horizontal lines indicate the target energy shown in Extended Data Table 1.

https://doi.org/10.1038/s41567-024-02751-2

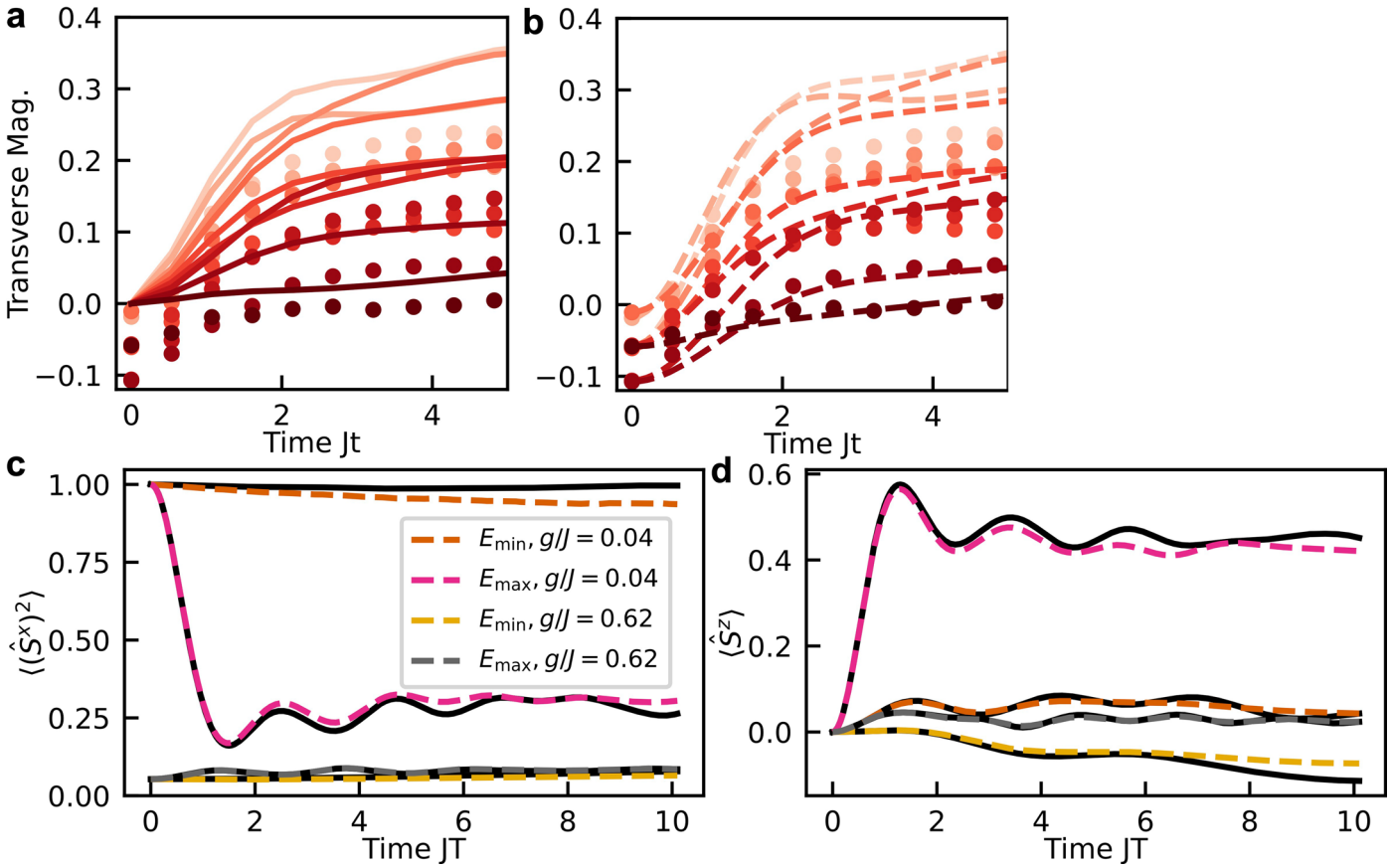

Extended Data Fig. 3 | Simulation of imperfections. a, Numerical simulations of the transverse magnetization $\sum_i \langle \hat{\sigma}_i^z \rangle / L$ using the same J_{ij} as the experiment (solid lines). **b**, Numerical simulation of the transverse magnetization $\sum_i \langle \hat{\sigma}_i^z \rangle / L$ using a tilted initial state (dashed lines, see text for definition). Dots in both subfigures are experimental data for the same initial states as shown in Fig. 2 of the main text. $g/J = 0.31$. $L = 13$. Numerical simulations including noise of **c**, Squared magnetization and **d**, Transverse magnetization. Black solid lines closest to data are corresponding noiseless results (that is not including the three noise sources discussed in the Methods, section "Influences of errors on the dynamics"), while dashed lines are the noisy results. We show dynamics of the two initial states with largest and smallest energy evolving under the smallest and largest magnetic field. We emphasize that this is the only figure that includes noise in the numerics; all other numerics are noiseless.

https://doi.org/10.1038/s41567-024-02751-2

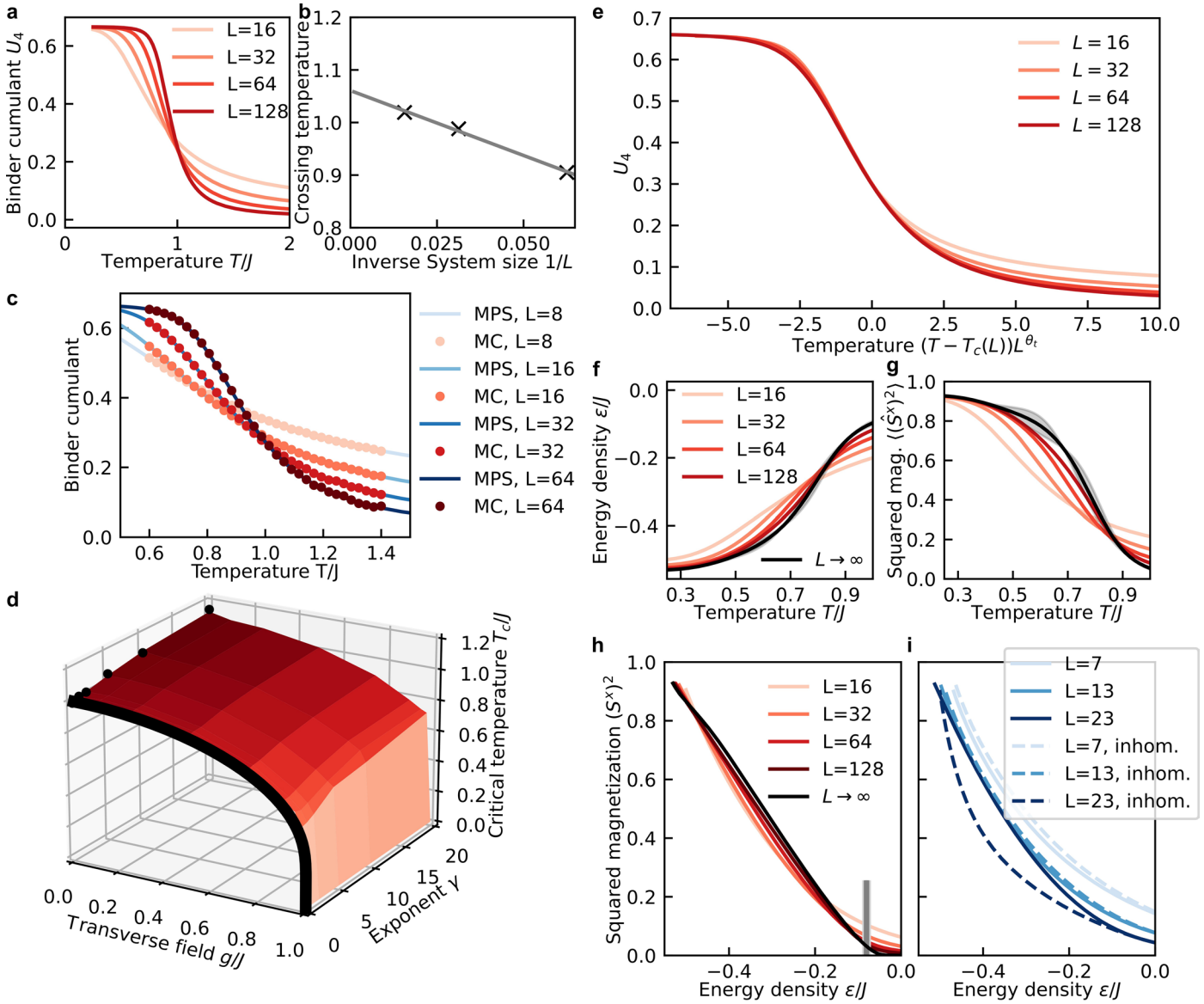

Extended Data Fig. 4 | Finite-energy phase diagram. a, Binder cumulant from purification-MPS for different system sizes. **b**, Crossing temperature of two consecutive system sizes. X-axis is defined as the smaller of the two. Bond dimension 16, time step $0.01/J$, $\gamma = 10.8$, $g/J = 0.25$. **c**, Verification of matrix-product-state simulations using classical Monte Carlo. Monte Carlo simulations employ a Wolff cluster update [59]for long-range interactions [60] and 10^6 Monte Carlo iterations. **d**, Phase diagram extracted from matrix-product-state simulations. System sizes up to $L = 128$ were used in the finite-size extrapolation described in the text. Black dots indicate classical Monte Carlo results for $g = 0$. Black solid line is the analytical mean-field result for $\gamma = 0$. **e**, Scaling collapse of the Binder cumulant. Same data as in subfigure a. $T_c(L)$ is chosen such that all system sizes cross at $T - T_c(L) = 0$. **f**, Energy density and **g**, Squared magnetization. The infinite-system-size extrapolation is using a quadratic fit to the finite-size results. $g/J = 0.25$. Gray shading is an estimate for the residual finite-size error obtained by comparing the extrapolation result using system sizes 16, 32, 64 and 16, 32, 64, 128. **h**, **i**, Finite-size behavior of energy-dependent squared magnetization. Solid lines are obtained from MPS simulations in the canonical ensemble using the target interactions defined in Eq. (1) of the main text. Transverse field $g/J = 0.25$, $\gamma = 10.8$, bond dimension $\chi = 16$. **h**, System sizes chosen as powers of two. The vertical gray line indicates the critical energy $E_c/J \approx -0.08$ obtained as described in section "Equilibrium phase diagram". The thickness of the light gray line indicates the uncertainty of the critical energy due to residual finite-size effects, defined as the difference in critical energy obtained from the infinite-system-size extrapolation using system sizes 16, 32, 64 and 16, 32, 64, 128. Dark gray shading is an independent estimate of the uncertainty resulting from the uncertainty in the critical temperature ($\pm 0.01J$). **i**, Experimentally probed system sizes using homogeneous interactions (full lines) using the inhomogeneous experimentally realized interactions, shown in Extended Data Fig. 1.

https://doi.org/10.1038/s41567-024-02751-2

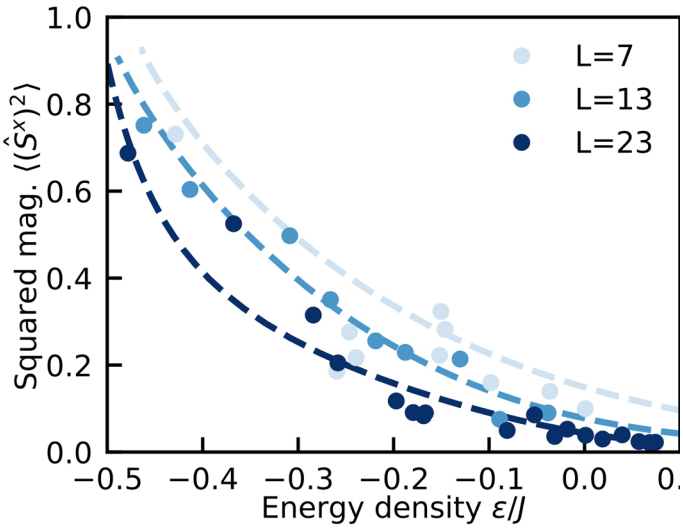

Extended Data Fig. 5 | Experimentally measured squared magnetization for different system sizes. Experimentally measured late-time squared magnetization (dots) compared to the numerical results in the canonical ensemble for the experimental J_{ij} (dashed lines, same as dashed lines in Extended Data Fig. 4i). $g/J = 0.24, 0.21, 0.18$ for $L = 7, 13, 23$, respectively.

https://doi.org/10.1038/s41567-024-02751-2

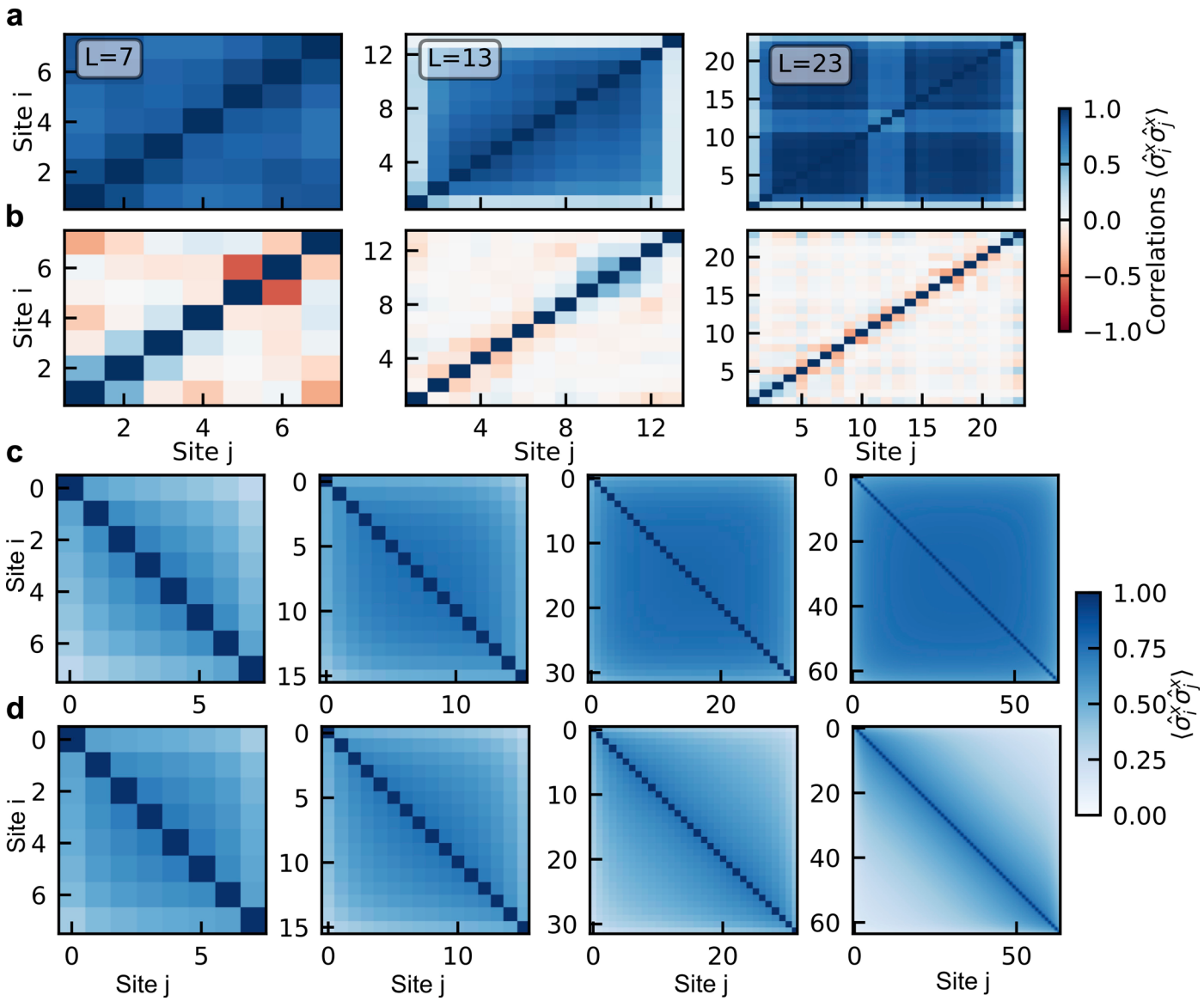

Extended Data Fig. 6 | Correlation functions. a, **b**, Correlation functions from numerical evaluation of time evolution with same parameters as Fig. 4 in the main text. First column: $L = 7$, second column: $L = 13$, third column: $L = 23$. **c**, **d** Matrix-product-state simulations of finite-temperature state. $g/J = 0.5$, temperature $T/J = 0.25$, bond dimension 16, time step $0.01/J$. System size 8, 16, 32, 64 increasing from left to right. In c, d we use the interactions J_{ij} in the main text, $J_{ij}^{\text{unnormalized}}$ defined in Eq. (S3) respectively. We find that the correlations decay faster as system size is increased when the interactions are not normalized, indicating the absence of long-range order.

https://doi.org/10.1038/s41567-024-02751-2

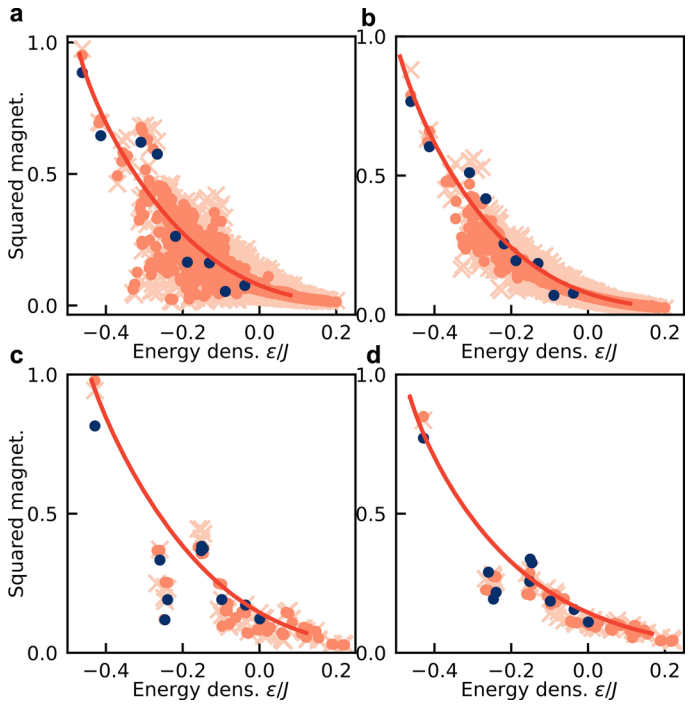

Extended Data Fig. 7 | Thermalization of all x-product initial states. Obtained from noiseless numerics evolved to the experimental latest time (crosses) and infinite time (orange dots). Blue dots are the latest time points of the time averaged experimental data. **a**, L=13, $g/J = 0.1$, **b**, L=13, $g/J = 0.21$, **c**, L=7, $g/J = 0.12$, **d**, L=7, $g/J = 0.24$.

https://doi.org/10.1038/s41567-024-02751-2

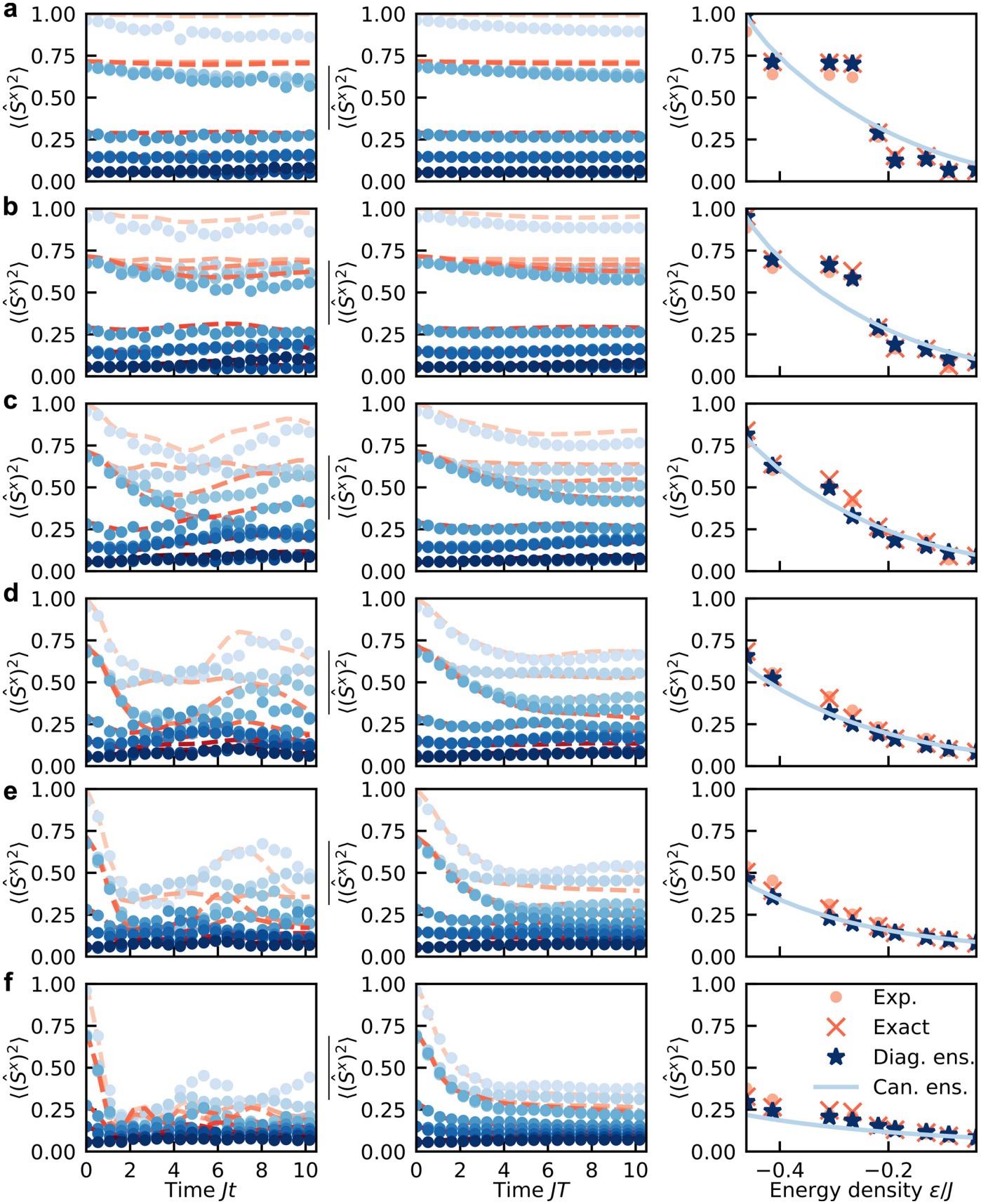

Extended Data Fig. 8 | See next page for caption.

https://doi.org/10.1038/s41567-024-02751-2

Extended Data Fig. 8 | Verification of equilibration. Same plot as Fig. 2 of main text for all transverse fields shown in Fig. 3 of the main text. The transverse field is fixed for each row and increases from top to bottom: $g/J = 0.04$ (**a**), 0.10 (**b**), 0.21 (**c**), 0.31 (**d**), 0.41 (**e**), 0.62 (**f**). $g/J = 0.31J$ corresponds to Fig. 2 of the main text, which we repeat here for completeness. System size $L = 13$. First column: time-evolved squared magnetization in the experiment (dots) and numerical simulations (dashed lines). Second column: time-average (up to time T) of the time-evolved squared magnetization using the data from the first row (dots) and the corresponding numerical data (dashed lines), evaluated according to Eq. 2 of the main text. Third column: comparison of the latest-time experimental data points from the second column (dots), numerical data evolved until the experimental time (crosses) and to infinite time, that is the diagonal ensemble (stars, evaluated according to the RHS in Eq.(S4)). The expectation from the canonical ensemble is shown as a solid line. The numerics use the experimentally realized interactions. $L = 13$, $g = 0.31J$. Error bars for the experimental data are quantum projection noise and are smaller than the point size.

https://doi.org/10.1038/s41567-024-02751-2

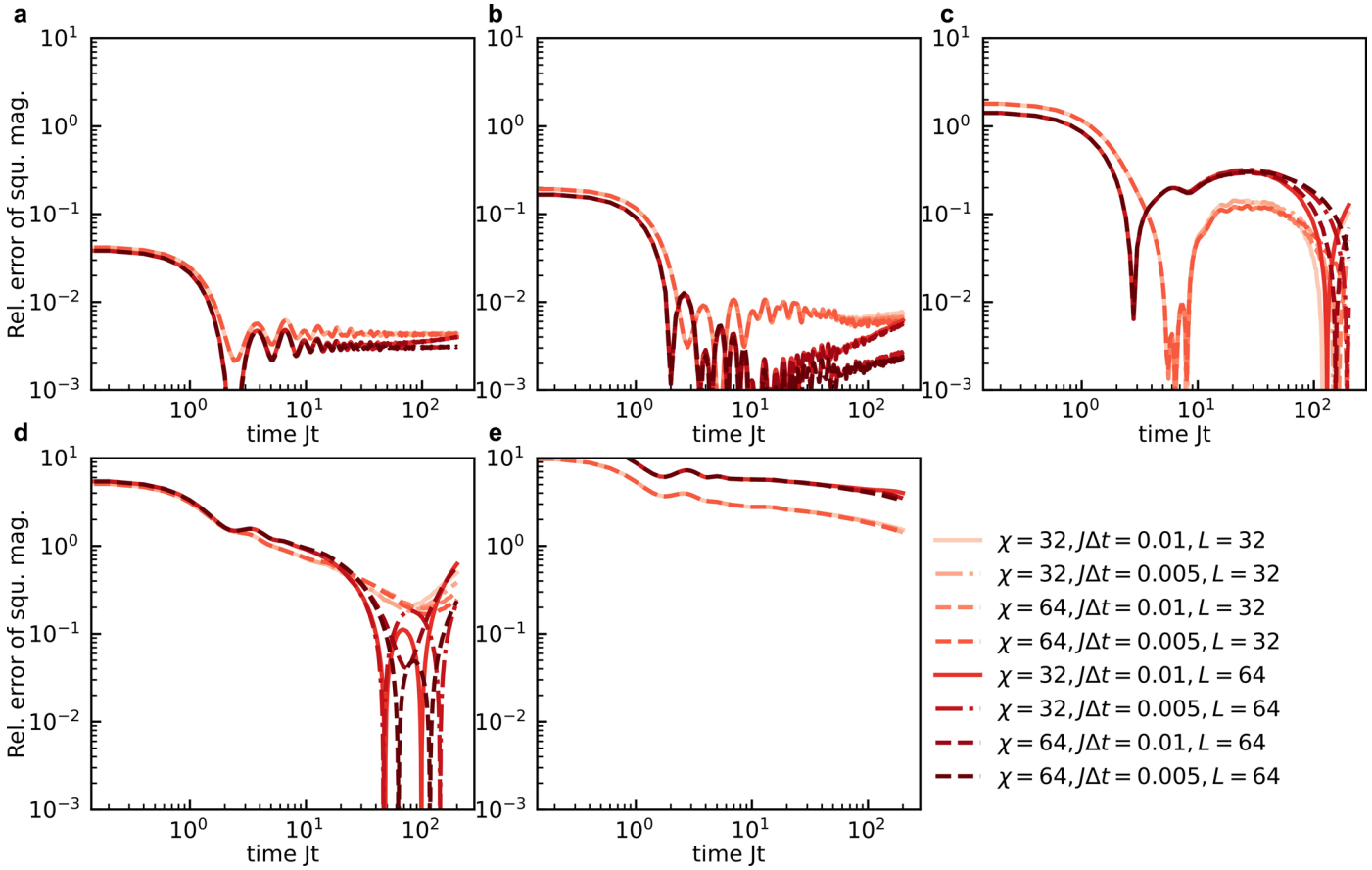

Extended Data Fig. 9 | Test of thermalization for large systems. Matrix-product-state simulations for the totally polarized initial state using bond dimension χ and imaginary time evolution step Δt. $\gamma = 10.8$. $g/J = 0.125, 0.25, 0.5, 0.625, 0.75$ for **a**, **b**, **c**, **d**, **e**, respectively.

https://doi.org/10.1038/s41567-024-02751-2

Extended Data Table 1 | Table of initial states

a

Energy density ϵ/J	State
-0.43	↓↓↓↓↓↓↓
-0.26	↓↓↓↓↓↓↑
-0.25	↓↓↓↓↓↑↓
-0.24	↓↓↓↓↓↑↑
-0.152	↓↓↓↓↑↓↓
-0.151	↓↓↓↓↑↓↑
-0.146	↓↓↓↓↑↑↓
-0.1	↓↓↓↓↑↑↑
-0.04	↓↓↓↑↓↓↓
0.0008	↓↓↓↑↓↓↑

b

Energy density ϵ/J	State
-0.46	↓↓↓↓↓↓↓↓↓↓↓↓↓
-0.41	↓↓↓↓↓↓↓↓↓↓↓↓↑
-0.31	↓↓↓↓↓↓↑↓↓↓↓↓↓
-0.27	↓↓↓↓↓↓↓↓↓↑↓↓↓
-0.22	↓↑↑↑↑↑↓↑↑↑↑↑↓
-0.19	↓↓↓↑↑↓↑↑↑↑↑↑↑
-0.13	↓↓↓↑↑↑↑↑↓↑↑↑↑
-0.09	↓↓↑↓↑↑↑↑↓↓↓↓↓
-0.04	↓↑↓↓↑↑↓↓↑↑↑↑↑

c

Energy density ϵ/J	State
-0.48	↓↓↓↓↓↓↓↓↓↓↓↓↓↓↓↓↓↓↓↓↓↓↓
-0.36	↓↓↓↑↓↓↓↓↓↓↓↓↓↓↓↓↓↓↓↓↓↓↓
-0.28	↓↓↓↓↓↓↓↓↓↓↓↓↓↓↓↓↓↑↑↓↓↓
-0.25	↓↓↓↓↓↑↑↓↑↓↓↓↓↓↓↓↓↓↓↓↓↓
-0.20	↓↓↓↓↑↑↓↓↑↑↓↑↓↓↓↓↓↓↓↓↓↓
-0.18	↓↓↓↑↓↓↑↑↓↓↓↑↑↓↓↓↓↓↓↓↓↓
-0.169	↓↓↓↑↓↓↓↑↑↓↓↓↑↑↓↓↓↓↓↓↓↓
-0.167	↓↓↓↑↑↓↓↑↑↓↓↑↑↓↓↓↓↓↓↓↓↓
-0.08	↓↓↓↓↑↑↓↓↑↑↓↓↑↓↓↑↓↓↓↓↓↓
-0.05	↓↓↓↑↓↓↓↓↓↓↓↑↑↓↑↓↓↑↑↓↑↓
-0.03	↓↓↓↓↑↓↓↑↑↓↓↑↓↑↑↓↓↓↓↓↑↑↑
-0.02	↓↓↓↑↓↓↑↓↓↑↓↑↑↑↑↑↑↑↓↓↑↑↓
0.001	↓↓↓↓↓↓↑↑↓↓↓↑↑↓↑↓↓↑↑↓↓↑
0.02	↓↓↓↑↓↓↓↓↑↑↓↑↑↑↓↓↑↑↓↓↑↑↓
0.04	↓↓↓↓↑↓↓↑↑↓↓↑↓↓↑↓↓↑↓↑↓↓↓
0.05	↓↓↓↓↑↑↓↓↑↑↑↑↓↑↓↑↑↓↓↑↑↓↑
0.0679	↓↓↓↑↑↓↓↑↑↓↓↑↑↓↓↓↑↑↓↑↑↓↑
0.0683	↓↓↓↓↑↑↓↓↑↑↓↑↓↓↑↓↓↑↑↓↓↑↑
0.074	↓↓↓↑↑↓↓↑↑↓↓↑↑↓↓↓↑↑↓↓↑↑↓

a, Initial states for $L = 7$. **b**, Initial states for $L = 13$. **c**, Initial states for $L = 23$. States are eigenstates of $\hat{\sigma}_l^x$.